4.1 Introduction

The Ruddlesden Popper (RP) phases can be written as $A_{n+1}B_nO_{3n+1}$, where n = 1 corresponds to A_2BO_4, n=2 to $A_3B_2O_7$, and the last member of this family is $n=\infty$ to ABO_3, [194]. The RP oxides shown interesting physical properties such as superconductivity, magnetoresistance, and mixed ionic and electronic conductivity [184–188], which are beneficial for energy and electronic devices. Extensive studies on the properties of A_2BO_4 phase have been carried out. Properties of rare earth based Ln_2NiO_4 (Ln=La, Pr, Nd) have been investigated in detail to make them useful as electrode (cathode/anode) material in solid oxide fuel cell (SOFC) [98, 118, 194]. However, its properties have been further improved by partially substituting alkaline earth metals (Ba, Sr, Ca) [85, 96, 101, 195].

Alkaline earth orthostannate, Ba_2SnO_4 and Sr_2SnO_4 have K_2NiF_4 -type tetragonal structure and space group **I4/mmm** [173]. The lattice parameters for Ba_2SnO_4 are a=b= 4.1411 Å and c=13.2834 Å and Sr_2SnO_4 are a=b=4.037 Å and c=12.530 Å [194]. UV-visible spectroscopy shows an optical transparency over the visible region with a direct transition of 3.18 eV for Ba_2SnO_4 and 4.6 eV for Sr_2SnO_4 [172]. Optical properties of Ba_2SnO_4 have been studied for its application in display devices [196, 197] and Photocatalytic activity [198, 199]. It has been reported that Ba_2SnO_4 crystallizes into undistorted tetragonal structure in which larger cation Ba has co-ordination number nine. On the other hand, coordination number of Sr in Sr_2SnO_4 get reduced to seven because of the titling of the SnO_6 octahedrons and leads to an orthorhombic distortion in the K_2NiF_4 structure at room temperature [125, 188].

It has been known that ABO_3 type perovskite oxides such as $BaTiO_3$ (BTO) and $SrTiO_3$ (STO) ; $BaSnO_3$ (BSO) and $SrSnO_3$ (SSO) form a complete solid solution [200, 201]. The properties of solid solutions have been found superior than that of their end members [67, 202, 203]. Therefore, in this work an attempt has been made to synthesize solid solutions of $Sr_{2-x}Ba_xSnO_4$ (with x= 0.2, 0.4, 0.8, 1.60 and 2.0) by solid state reaction route. In this system, the valence state of Sr and Ba is same whereas the difference in the ionic radii is less than 15 %. So, Hume-Rothery condition suggests the possibility of solid solutions exist in wide range. To verify experimentally, the above-mentioned compositions of system $Sr_{2-x}Ba_xSnO_4$ are synthesized.

4.2 Results and Discussion

In this chapter, the synthesized compositions of $Sr_{2-x}Ba_xSnO_4$ with x=0, 0.2, 0.4, 0.8, 1.6 and 2.0 abbreviated as SSB0, SSB1, SSB2, SSB4 SSB8 and SSB10 respectively.

4.2.1 Phase Formation and Structural Characterization using XRD

The XRD pattern of synthesized Sr_2SnO_4 powders calcined at 1000^oC for 8h are shown in Figure 4.1(a). The diffraction peaks have been indexed using standard COD files of Sr_2SnO_4 [173], which reveal the formation of single phase materials. Further incorporation of Sr at Ba site has been probed by X-ray diffraction peak corresponding to (103) and (110) planes observed at 30.74^o and 31.30^o are shown in Figure 4.1(b). The shift in position of XRD peaks towards lower angle (2θ) side has been observed with increasing composition of Ba, which might be due to higher ionic radii of Ba (1.47 Å) than Sr (1.31 Å). The substitution of higher ionic radii Ba at Sr^{2+} site shifts the XRD peak towards lower angle; also it pronounced the expansion of the Unit Cell. The formation of single phase powder for all investigated compositions indicates that both the end members Sr_2SnO_4 and Ba_2SnO_4 are mutually soluble into each other. This result is in contrast to the result reported on $Ba_{2-x}Sr_xFeO_{4+\delta}$, for which single phase solid solutions were obtained for selected compositions only [210]. While another report on Ba substituted Sr_2TiO_4 by A. K. Ganguly et al., it has been reported that Ba is not completely soluble at Sr site of Sr_2TiO_4 [211]. In the present case, the mutual solubility of both the phases is may be due to similar crystal structure of Ba_2SnO_4 and Sr_2SnO_4.

However, in case of the solid solution of Ba_2TiO_4/Sr_2TiO_4 and $Ba_{2-x}Sr_xFeO_{4+\delta}$, it belongs to different crystal structure and space group.

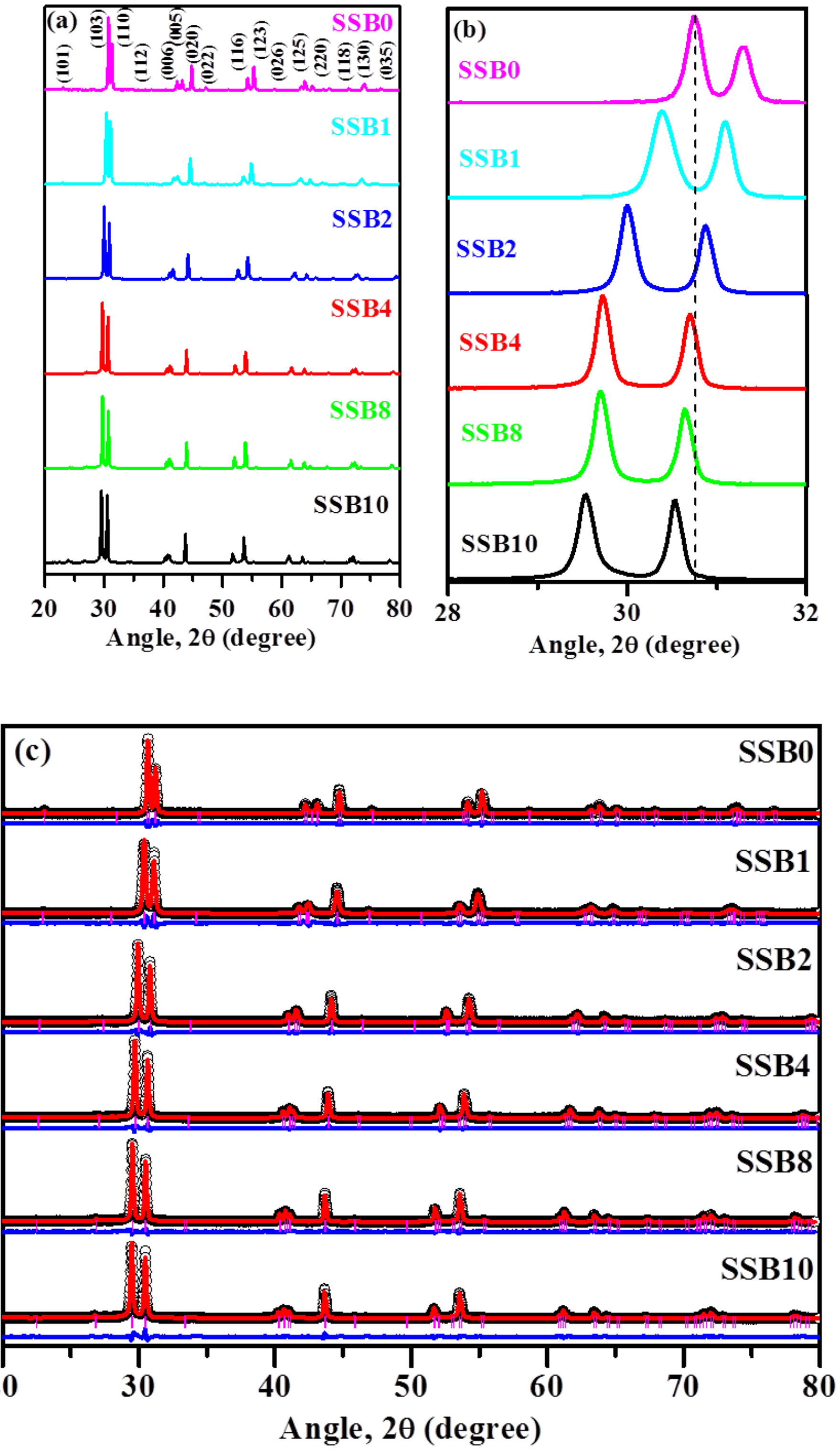

Figure 4.1 (a) Room temperature powder X-ray diffraction pattern of prepared samples and (b) enlarge view of (116) and (123) diffraction peak (c) Room temperature XRD pattern refined using the Rietveld method.

To determine the structural parameters and the stability of crystal structure by incorporating Ba at the Sr site, Rietveld refinement of XRD data has been carried out using **FullProf software suite.** The refined pattern of solid solutions is shown in Figure 4.1(c). Detailed procedure of Rietveld refinement is already discussed in Chapter 3. The goodness of fit parameter (S) for Reitveld refinement is calculated using the value of reliability parameters (R_{wp} and R_p) through relation $S = \frac{R_{wp}}{R_p}$. The value of reliability factors are consistent with the values reported in the literature for similar types layered perovskites [205, 206]. The structural parameters such as lattice parameter, unit cell volume, density bond length and bond angle obtained from the refinement are given in Table 4.1. From Table 4.1, it is noticed that the bond length associated with Sr atom i.e., Sr/Ba-Sn, Sr/Ba-O2, Sr/Ba-O1 found to be increased with increasing the composition of Ba and takes part in the expansion of unit cell. The crystal structure of the samples after refinement is obtained using the **VESTA Software** for sample SSB4 [213] is shown in the inset of Figure 4.2(a) as a reference. From the structure, it is clear that Ba/Sr has occupied the corner position in the perovskite unit cell and centered position in Ba/SrO layer whereas Sn occupied body-centered (BC) position in the perovskite unit cell. The position of oxygen along c-axis and along a $(= b)$ axis in perovskite unit cell is denoted as O1 (equatorial position) and O2 (apical position) respectively (Figure 1.3). The value of tolerance factor theoretically calculated (as given in Table 4.1) using relation $t = \frac{(1-x)r_{Ba}+xr_{Sr}+r_O}{\sqrt{2}(r_{Sn}+r_O)}$ is accordance with experimental results obtained from Reitveld refinement studies. Figure 4.2(b) depicts the variation of the lattice parameters (a, b and$c$) with Sr concentration. The experimental data points are linearly fitted with composition of Sr is given by following equation;

$$a = b = 0.04937x + 4.1466\ (\text{Å}) \text{ and } c\ =\ 0.35621x + 13.3204\ (\text{Å}) \qquad (4.1)$$

Where, a, b and c represent lattice parameters and x is the percentage of Ba content. With increasing Ba both the parameters a and c increased linearly, and the ratio of c/a also increases. The variation in structural parameters should be related to the radius of ions as well as the variation of their content.

Table 4.1 Parameters obtained after refinement, cell volume, density, atomic coordinates, atomic occupancy, tolerance factor (experimental, calculated), various bond lengths and bond angles for solid solutions.

S. No.		**SSB1**	**SSB2**	**SSB4**	**SSB8**	**SSB10**
Lattice Parameters	a (Å)	4.0662(5)	4.1022(4)	4.1237(6)	4.1441(5)	4.1458(3)
	c(Å)	12.7660(10)	13.0420(11)	13.1780(9)	13.2732(9)	13.2899(2)
c/a		3.13954	3.17927	3.19567	3.20291	3.20563
Cell volume (Å^3)		211.07	219.46	224.08	227.95	228.42
Density (gm/cm^3)		5.90	6.43	6.73	6.86	7.53
R_p		7.6	6	5.6	4.4	4.3
R_{wp}		8.1	6.7	6.4	5.3	5.5
$S=R_{wp}/R_p$		1.06	1.11	1.13	1.2	1.27
R_{Bragg}		2.50164	1.9105	2.24182	2.99727	3.07311
χ^2		5.6	3.96	3.28	3.62	5.72
Atomic Co-ordinate						
Ba		(0,0,0.35236)	(0,0,0.35217)	(0,0,0.35234)	(0,0,0.35270)	(0,0,0.35235)
Sr		(0,0,0.35236)	(0,0,0.35217)	(0,0,0.35234)	(0,0,0.35270)	_
Sn		(0,0,0,)	(0,0,0,)	(0,0,0,)	(0,0,0,)	(0,0,0,)
O1		(0.5,0,0)	(0.5,0,0)	(0.5,0,0)	(0.5,0,0)	(0.5,0,0)
O2		(0,0,0.15202)	(0,0,0.16394)	(0,0,0.15257)	(0,0,0.15968)	(0,0,0.14636)
Occupancy						
Ba		0.41572	1.19076	1.5807	1.78054	1.99888
Sr		1.59833	0.79964	0.39969	0.19286	_
Sn		1	1	1	1	1
O1		2.12543	2.09803	2.09466	2.10397	2.14613
O2		1.87423	1.87923	1.87032	1.83072	1.83016
Crystallite Size (nm)		27.56	28.64	29.13	29.03	36.92
Tolerance factor (Th.)		0.937	0.951	0.953	0.962	0.975
Tolerance factor (Exp.)		0.96	0.965	0.968	0.97	0.972
Bond length (Å)	Ba/Sr-Sn	3.43165(11)	3.48298(6)	3.50552(5)	3.5227(5)	3.5292(3)
	Ba/Sr-O2	2.417(2)	2.45490(8)	2.632(10)	2.56211(6)	2.7015(5)
	Ba/Sr-O1	2.76455(11)	2.81499(6)	2.83505(2)	2.84832(5)	2.8569(3)
	Sn-O2	2.0331(8)	2.0510(7)	2.0618(3)	2.0720(6)	2.0729(4)
	Sn-Sn	4.0662(2)	4.1021(8)	4.1236(5)	4.1441(3)	4.1458(6)
Bond Angle (degree)	Sr-Sn-O2	123.08	123.61	123.68	123.71	123.8
	O2-Sn-O1	90	90	90	90	90

As discussed above the ionic radii of Ba^{2+} is larger than Sr^{2+} in the same coordination state, which leads to increase in both lattice parameters. The lattice parameters is found to be linearly dependent on the composition of Ba and the rates of expansion along c-axis and a-axis are 0.44 and 0.14 Å. Obviously, c-axis along the z direction of unit cell presents a expansion larger than a, b-axis. The different expansion ratio of c- and a-axis can be understood by the special lattice structure of layered perovskite Sr_2SnO_4 in which a number of Sr sites along c-axis is higher as compared to that along a and b axis [See Figure 4.2(a)].

The broadening in the X-ray diffraction peak measured experimentally (β_{total}) has a major contribution of crystallite and instrumental broadening. Therefore, to get an accurate value of crystallite size, the contribution of instrumental broadening must be subtracted from the total broadening as recorded experimentally. In order to correct the instrumental broadening, standard sample (Si-single crystal) has been used. The value of β_{sample} was obtained using Eq. (4.2);

$$\beta_{sample}{}^{2} = \beta_{total}{}^{2} - \beta_{Si}{}^{2} \tag{4.2}$$

Using value of β_{sample} , the crystallite size has been calculated for most intense X-ray diffraction peak (013) plane using Scherer's formula given by Eq. (2.15) and listed in Table 4.1. From Table 4.1, it is noticed that the crystallite size increases with increasing concentration of Ba in the solid solution which is ascribed to larger ionic radii and higher unit cell volume on Ba substitution compared to SSB0.

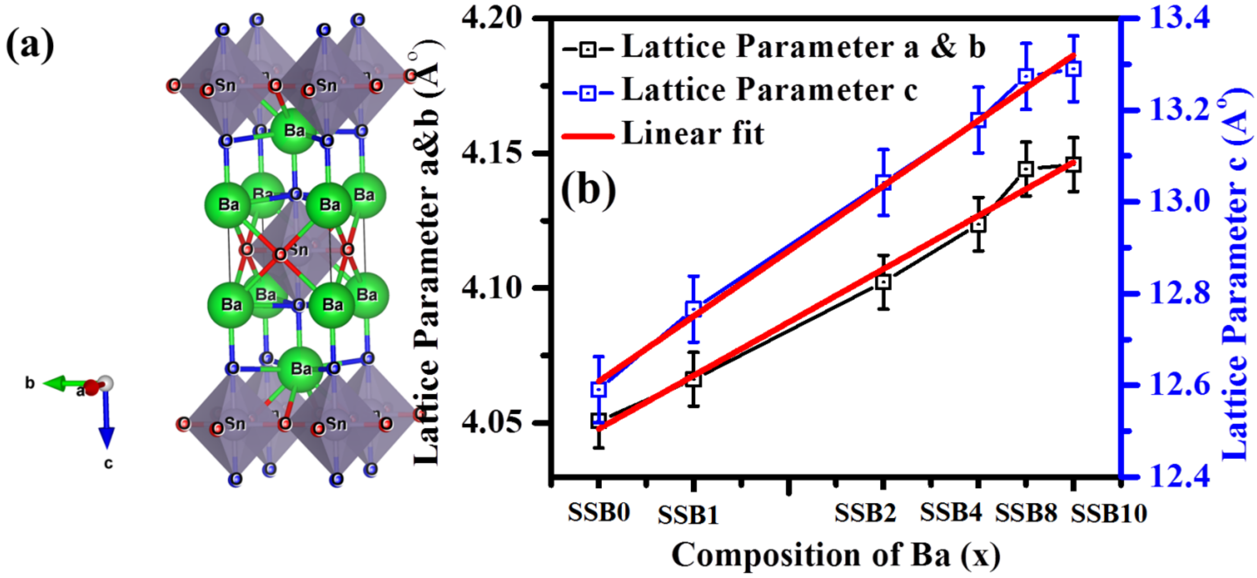

Figure 4.2 (a) Structure of prepared solid solution SSB2 (b) Variation of lattice parameter a, b, c with respect to the composition of Sr.

4.2.2 Fourier Transform Infrared Spectroscopy analysis

In order to further reconfirm the incorporation of Ba into the lattice as well as to analyze the presence of functional group, FTIR spectroscopy technique has been used. Figure 4.3 depicts FTIR spectrum of all the samples. The FTIR spectrum of both end members Sr_2SnO_4 and Ba_2SnO_4 are well matched with the reported FTIR spectra of Ba_2SnO_4 (SSB10) and Sr_2SnO_4 (SSB0) [176, 208]. Positions of all the bands observed in the samples are given in Table 4.2. On incorporation of Ba at Sr site the effective mass and bond length increased which brings shift in the position of characteristic bands. In the FTIR spectrums of solid solutions, the positions of all bands are listed in Table 4.2 (Figure 4.2(a)). The band observed at 542 cm^{-1} associated with Sr-O shifts towards slight higher wavenumber with Ba, further it is noticed that with the incorporation of Ba another band is observed towards higher wave number which may be due to presence of Ba-O band. Moreover the position of another characteristic band associated with Sn-O is shifted towards lower wavenumber from 707 to 626 cm^{-1} for sample SSB0 to SSB10 respectively which may be due to increase in bond length of Sn-O. A weak band observed at 856 cm^{-1} is assigned to the formation of alkaline earth carbonates. The formation of carbonates may takes place by adsorption of CO_2 gas present in the atmosphere [214].

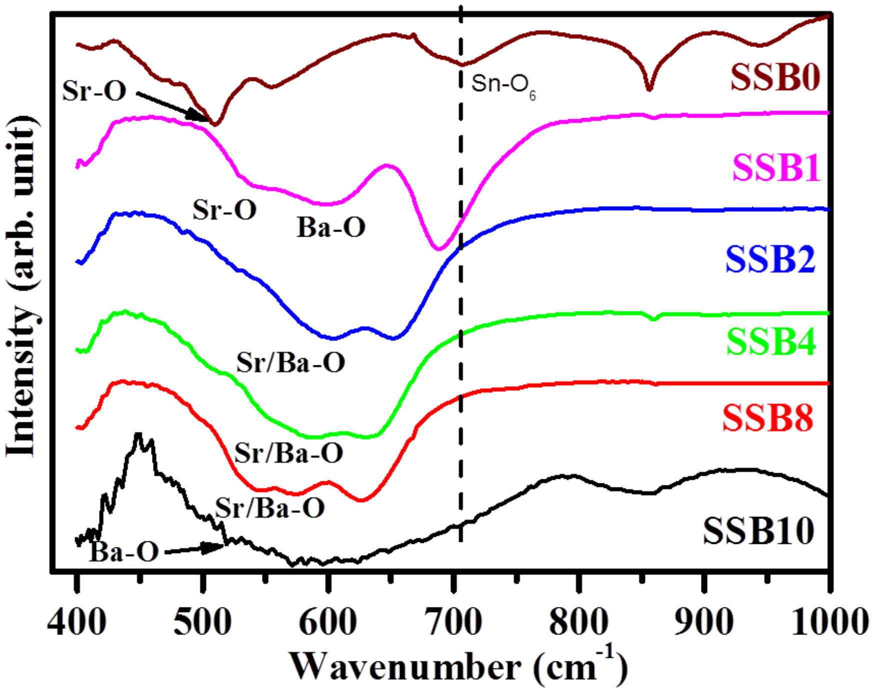

Figure 4.3 Fourier Transform Infrared (FTIR) spectra of all samples.

Table 4.2 Position of bands present in the samples.

Sample code	**Position of bands (cm^{-1})**
SSB1	542, 597, 690, 861
SSB2	541, 603, 652, 852
SSB4	548, 585, 635, 854
SSB8	546, 576, 628, 851
SSB10	518, 626, 856

4.2.3 Transmission Electron Microscopy (TEM) analysis

The particle size of a representative sample SSB2 is analyzed using TEM technique. The TEM image shown in Figure 4.4(a) reflects spherical shape of particles with uniform size. The average diameter of spherical particles is determined by the fitting of Gaussian function to the histogram generated for the distribution of particle size is shown in Figure 4.4(b). The average particle size is found to be (76 ± 5) nm. Value of the particle size is found to be higher than crystallite size which indicates that the particles consist of almost two crystallites. Selected area electron diffraction (SAED) pattern of the sample is shown in Figure 4.4(c). Bright spots in the form of circular rings insure polycrystalline nature of powder. These rings are belonging to the different Miller planes (h, k, l) indexed in Figure 4.4(c). The High-resolution TEM image of sample is also obtained and illustrated in Figure 4.4(d). Fine parallel lines in different orientations are observed which can be assign to different Miller planes of sample. The distances between two successive parallel lines of same orientation are calculated by **Image J** software. The calculated d values are 1.7394 Ǻ, 2.0510 Ǻ, 2.2011 Ǻ and 2.9068 Ǻ assigned to (116), (200), (105) and (013) planes of Sr_2SnO_4 consistent with XRD results.

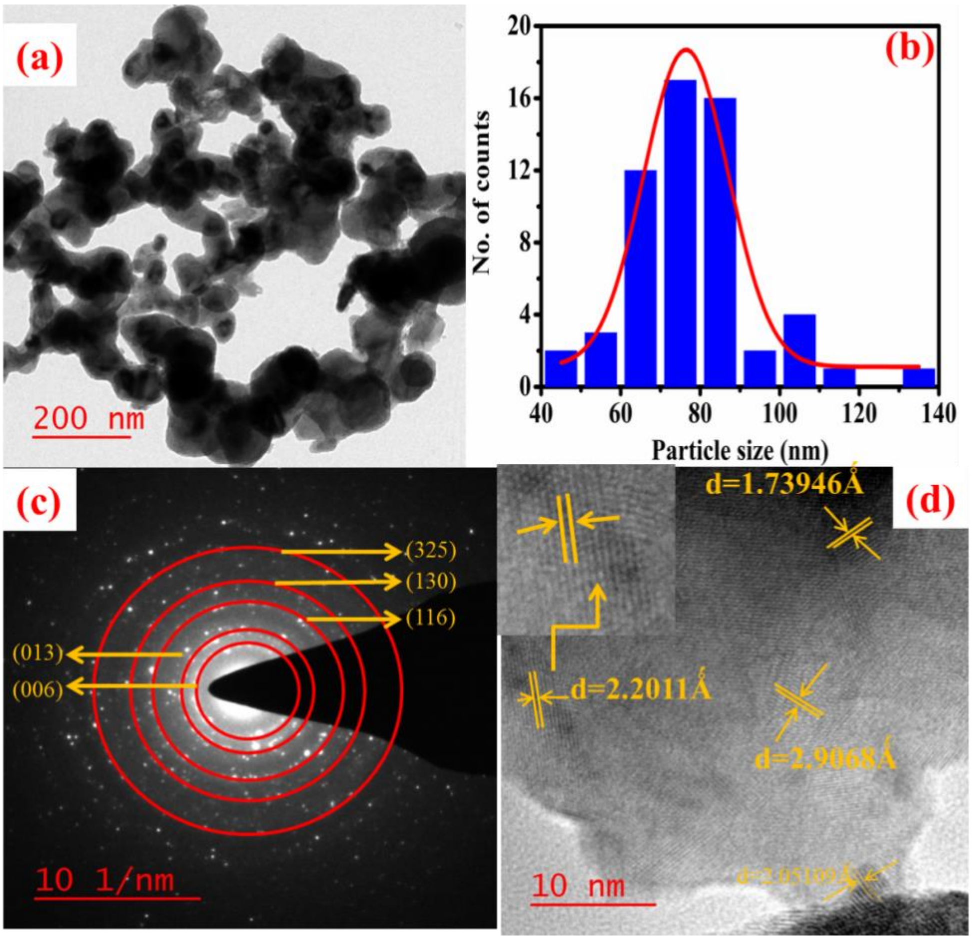

Figure 4.4 (a) Bright field TEM image (b) Histogram of distribution of particle size (c) (SAED) pattern and (d) High-resolution transmission electron image of the sample SSB2.

4.2.4 Microstructural study using FESEM

The morphology of freshly fractured surfaces of sintered pellets has been studied by FESEM. Scanning electron micrograph (SEM) of all the samples is recorded at constant magnification 50,000 and shown in Figure 4.5(a-f). The grains are found to be spherical which is consistent with the literature [215]. **Image J** software is used to determine the average grain size. The histograms of distribution in grain size for samples are obtained and shown in Figure 4.6(a-f). The average grain size of the samples is determined by Gaussian fitting to the Histogram. It is noticed that both size and degree of agglomeration of the grains increases with increase of Ba in the solid solution.

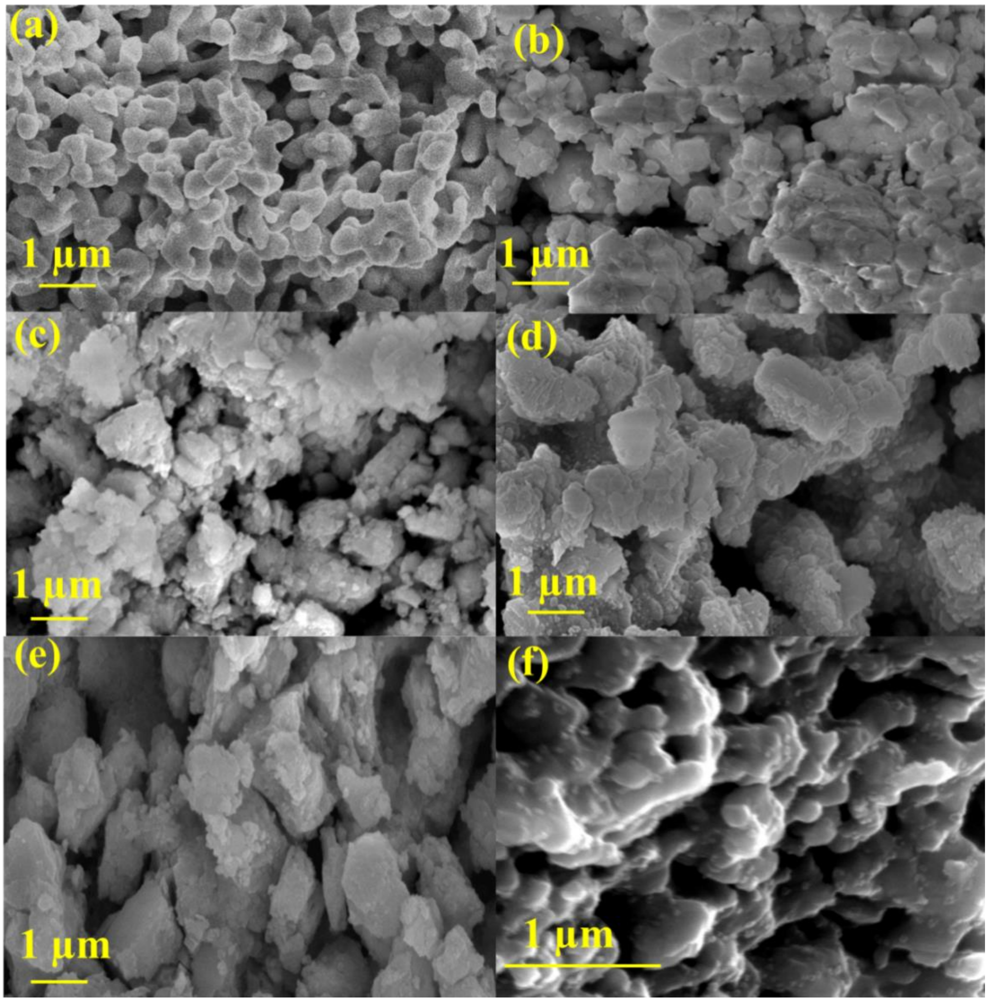

Figure 4.5 High-Resolution Scanning electron micrograph of freshly fractured surface of the sintered pellets (a) SSB0 (b) SSB1 (c) SSB2 (d) SSB4 (e) SSB8 (f) SSB10.

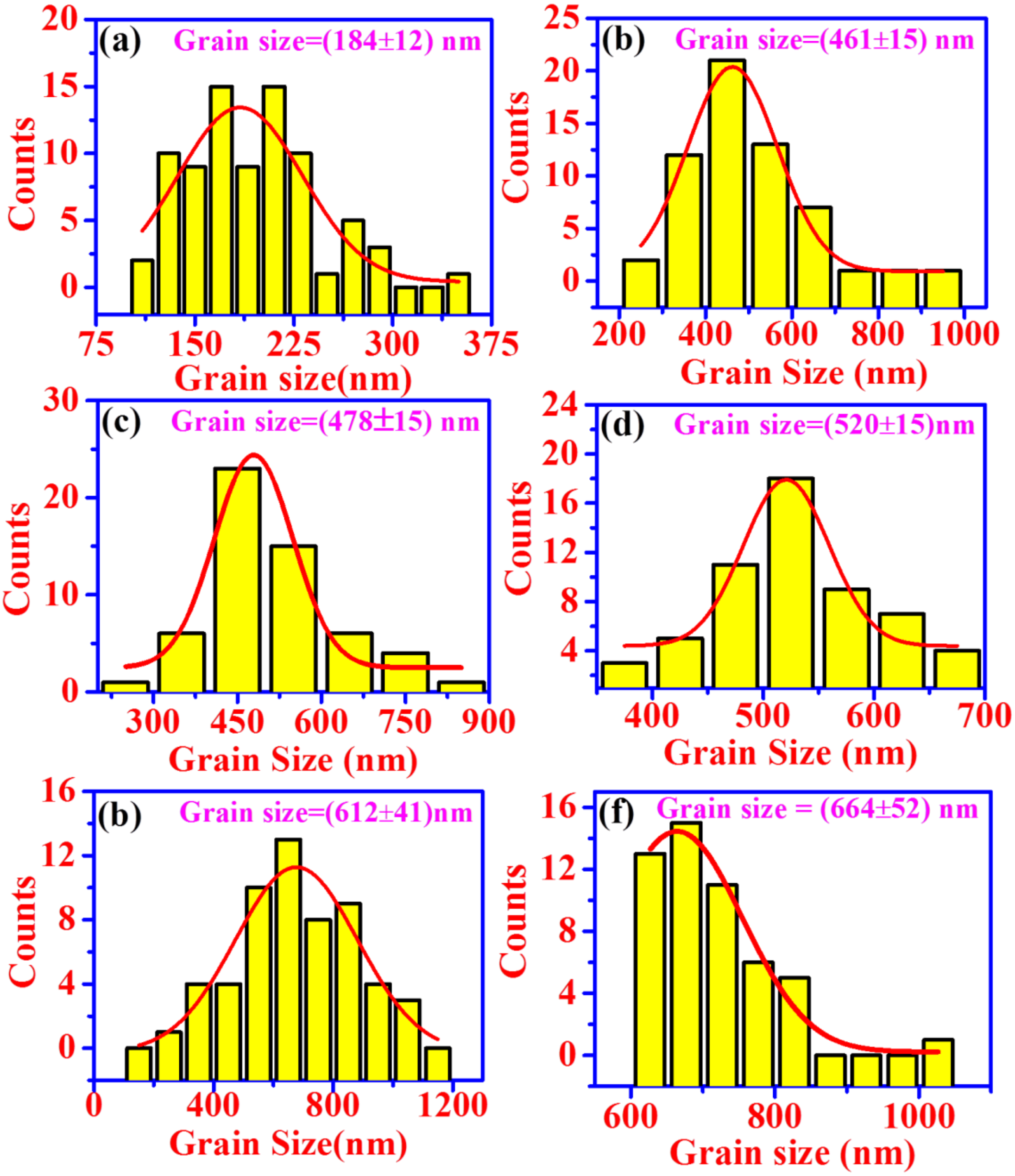

Figure 4.6 Histogram fitted with Gaussian function of sample (a) SSB0 (b) SSB1 (c) SSB2 (d) SSB4 (e) SSB8 (f) SSB10.

4.2.5 X-ray Photoelectron Spectroscopy (XPS) analysis

The X-ray photoelectron spectroscopy (XPS) measurements are performed to reveal the valance state of the elements present in the samples. The XPS survey scan spectrum for one of the representative sample SSB2 is shown in Figure 4.7(a). The survey scan report of the present sample is compared with XPS survey report of Sr_2SnO_4 [216]. On comparing with literature, it has been found that all the peaks belong to the binding energy of elements Ba(3d), Sr(3d), Sn(5d) and O(1s).

The High Resolution X-ray Photoelectron Spectrum (HRXPS) of the individual elements like Ba(3d), Sr(3d), Sn(5d) and O(1s) are shown in Figure 4.7(b), (c), (d), (e) respectively. The position of the peaks has calibrated against the C(1s) correction, whose binding energy is observed at 284.6 eV [217]. The high resolution XPS spectrum states corresponding to Ba (3d) shows doublet peaks centered at 779.03 and 794.35 eV corresponds to the state $3d_{5/2}$ and $3d_{3/2}$ respectively. The spin-orbit splitting energy between $3d_{5/2}$ and $3d_{3/2}$ state is 15.32 eV which is in agreement with the spin-orbit splitting energy for Ba^{2+} state [183, 217]. The HR-XPS of Sr (3d) shows the doublet peaks centered at 133.05 and 134.45 eV corresponding to the state $3d_{5/2}$ and $3d_{3/2}$. The observed peaks were well matched with Sr^{2+} state originating from Sr-O [216]. The HRXPS of Sn (5d) shows doublet peaks centered at 485.45 and 493.85 eV assigned to $5d_{5/2}$ and $5d_{3/2}$ states, respectively. Both the peaks show an asymmetry in their peak shape which indicates the presence of Sn in more than one valence state. In the literature, it is mentioned that in Sn-based perovskite oxides synthesized using high-temperature solid state method; Sn exists in both Sn^{4+} and Sn^{2+} state. Therefore, peak corresponding to $5d_{5/2}$ and $5d_{3/2}$ states are deconvoluted into two peaks centred at 485.20 and 493.60 eV for Sn^{2+} state and 485.90 and 494.30 eV for Sn^{4+} state corresponding to $5d_{5/2}$ and $5d_{3/2}$, respectively [211, 212]. On the other hand, HRXPS of O(1s) spectrum shows a single peak with small asymmetry towards higher as well as lower binding energy side which indicates the presence of different kind of oxygen may be related with the defects. In order to identify these defects, the peak is deconvoluted into three peaks which having centered at 529.50, 530.60 and 531.46 eV. These peaks are assigned to the interstitial oxygen, lattice oxygen and oxygen vacancies, respectively with the help of literature reports [210, 211, 213].

The formation of oxygen vacancies in the samples takes place during sintering at a high temperature because the samples in this study were synthesized via the solid state ceramic route at 1200°C. As discussed in Chapter 3, from Eq. (1.10) and (3.5), the presence of oxygen vacancies and reduction to valence state of Sn^{4+} can be seen.

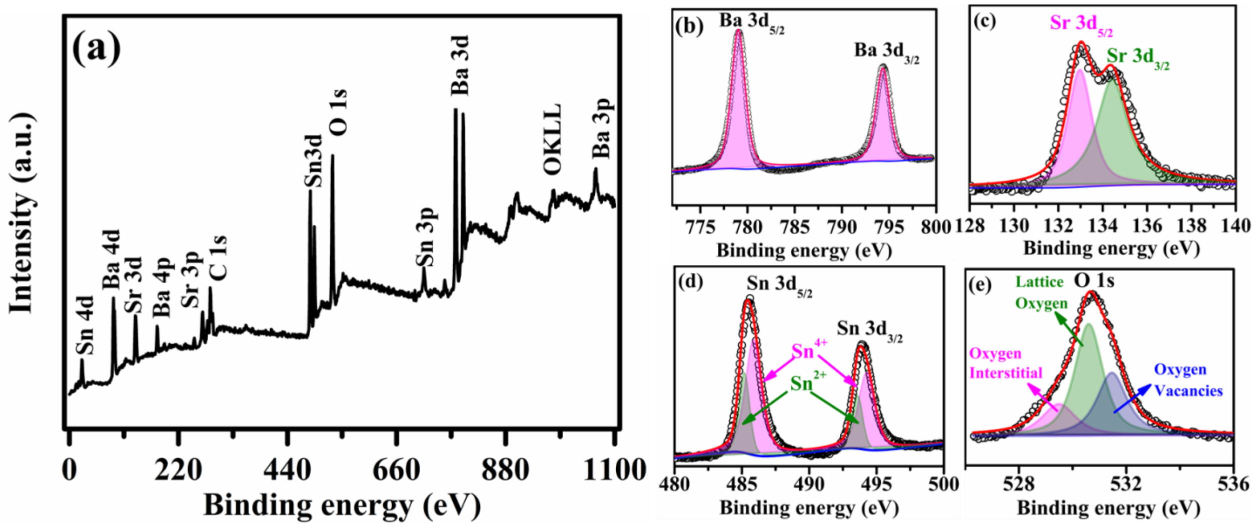

Figure 4.7 (a) X-ray photoelectron spectroscopy (XPS) survey scan report for sample SSB4, (b-e) fitted core level XPS spectrum of Ba, Sn, Sr and O elements.

4.2.6 Electrical Characterizations

The electrical properties of Ba_2SnO_4 has already been reported in literature [220] whereas Sr_2SnO_4 is already described in detail of this thesis Chapter 3. Therefore, in this section, experimental results of solid solution have been described. The frequency dependent dielectric constant, dissipation factor, real part of modulus, imaginary part of modulus and conductivity shows similar trends of variation. Therefore, in that case only the variation is shown for a reference sample SSB2.

4.2.6.1 Dielectric Spectroscopy analysis

Dielectric properties of sintered samples are measured in the temperature range 60- 600 °C and frequency range 20 Hz – 2 MHz. Figure 4.8(a) and (b) shows a variation of dielectric constant (ε_r) and dissipation factor (D) with temperatures at a constant frequency (10 KHz) of all the samples. It is observed that both dielectric constant and dissipation factor remains constant upto certain temperature 150°C, thereafter starts increasing on further increase in temperature. Furthermore, it is found that as content of Ba increases in the solid solution, the value of dielectric constant and dissipation factor at given temperature decreases. The overall dielectric properties of a polycrystalline ceramic materials are governed by four types of polarization, namely electronic, ionic, orientational and interfacial polarization [156]. The frequency range of their response of polarization is different. Interfacial polarization is observed in the frequency range 1 mHz to 10^3 Hz, orientational polarization between 10^3 to 10^6 Hz, ionic polarization in 10^6 to 10^9 Hz and the electronic polarization above 10^9 Hz. Therefore, in present frequency range only the contributions of two types of polarizations i.e., orientational and interfacial polarization similar to the other polycrystalline ceramics, glass ceramics is present [150,205,215]. It has been confirmed from the XPS studies of the sample SSB2 that Sn is present in both Sn^{2+} and Sn^{4+} states. Presence of Sn^{2+} at Sn^{4+} site is an acceptor $(Sn^{2+}{}_{Sn^{4+}})''$ which can form dipole with vacant oxygen sites ($V_O^{\cdot\cdot}$) namely ($Sn^{2+}{}_{Sn^{4+}}{}'' - V_O^{\cdot\cdot}$). These dipoles responded in presence of field by two ways; first by jumping of oxygen vacancy to another vacant site and second by the hopping of electron between Sn^{2+} to Sn^{4+} site after the certain temperature say above 150°C. It is suggested that the dielectric constant may be the major contribution of orientational polarization based on the available frequency.

The variation of dielectric constant and dissipation factor as a function of frequency for sample SSB2 is shown in Figure 4.8(c) and (d). Similar behavior is observed for other samples also. At lower frequency, the dielectric constant and dissipation factor is found to be 4000 and 6 respectively. With increasing frequency, the dielectric constant and dissipation factor is sharply decreased upto 10^4 Hz. A close view of dielectric constant and dissipation factor between 10^2 to 10^4 Hz are shown in the inset of Figure 4.8(c) and (d) respectively. It is noticed that with increasing temperature, dispersion is increased in the dielectric constant and dissipation factor and may be due to presence of Interfacial polarization in the sample. The Interfacial polarization is may be occurred due to microheterogeneity present at following regions:

- In the grain and grain boundaries.
- At the interface of grain and grain boundaries.
- Electrode-sample interface.

Since the material has been synthesized by a slow diffusion-controlled thermochemical process, so possibility of micro-heterogeneities present in the final product can not be ruled out. The chemical microhetrogeneity is the random occupation of similar sites by different ions which possess different microregions with varying in their conductivity. In present sample, the centered position of SnO_6 octahedra is randomly occupied by Sn^{2+} and Sn^{4+} ions (as deduced in XPS analysis) and Sr- sites are occupied by Ba^{2+} and Sr^{2+} ions. Because of these chemical micro-heterogeneities, the samples have different micro-regions with varying conductivity. These micro-regions may lead to interfacial polarization. The dissipation factor (D) found to be lower at high frequency and increased with decreasing frequency. Rapid increase in dissipation factor D at low frequency is due to DC conductivity. In addition, at higher frequencies, the time is lower and conductivity occurs only at local level, so that the dissipation factor is lower. Since the dielectric constant decreases as the composition of Ba increases, it may be due to either a decrease in the number of dipole or increased dipole separation. The XPS spectrum of a sample shown in Section 4.2.5 indicates the presence of oxygen interstitial in the sample which leads an excess negative charge in the sample shown by Eq. (1.8).

The presence of oxygen interstitial makes a neutral pair with oxygen vacancy as following;

$$O_i'' + V_O^x \rightarrow O_O^x \text{ (null)} \qquad (4.3)$$

$$Sn^{2+} + 2h^{\cdot} \rightarrow Sn^{4+} \qquad (4.4)$$

This neutral pair reduces the number of dipoles contributing to the dielectric constant resulting in the dielectric constant being decreased.

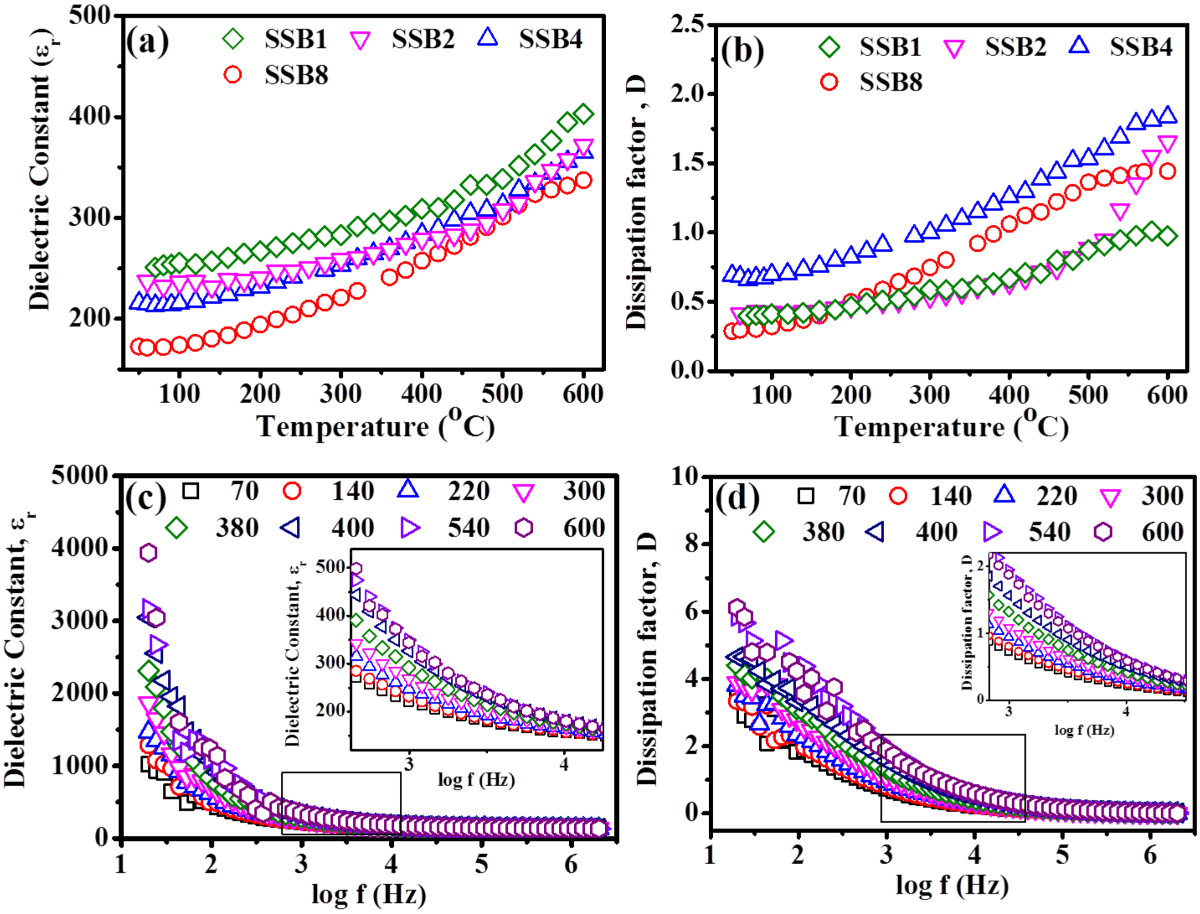

Figure 4.8 Variation of (a) dielectric constant (b) dissipation factor with temperature for solid solutions; Variation of (c) dielectric constant and (d) dissipation factor (D) against frequency at several temperatures (Temperature in °C).

4.2.6.2 Modulus Spectroscopy analysis

Modulus spectroscopy analysis has been carried out to understand the dielectric properties in depth. In the complex plane electric modulus formalism, M^* is expressed in terms of complex dielectric constant (ε^*) as given by Eq. (3.8) and (3.9) [222].

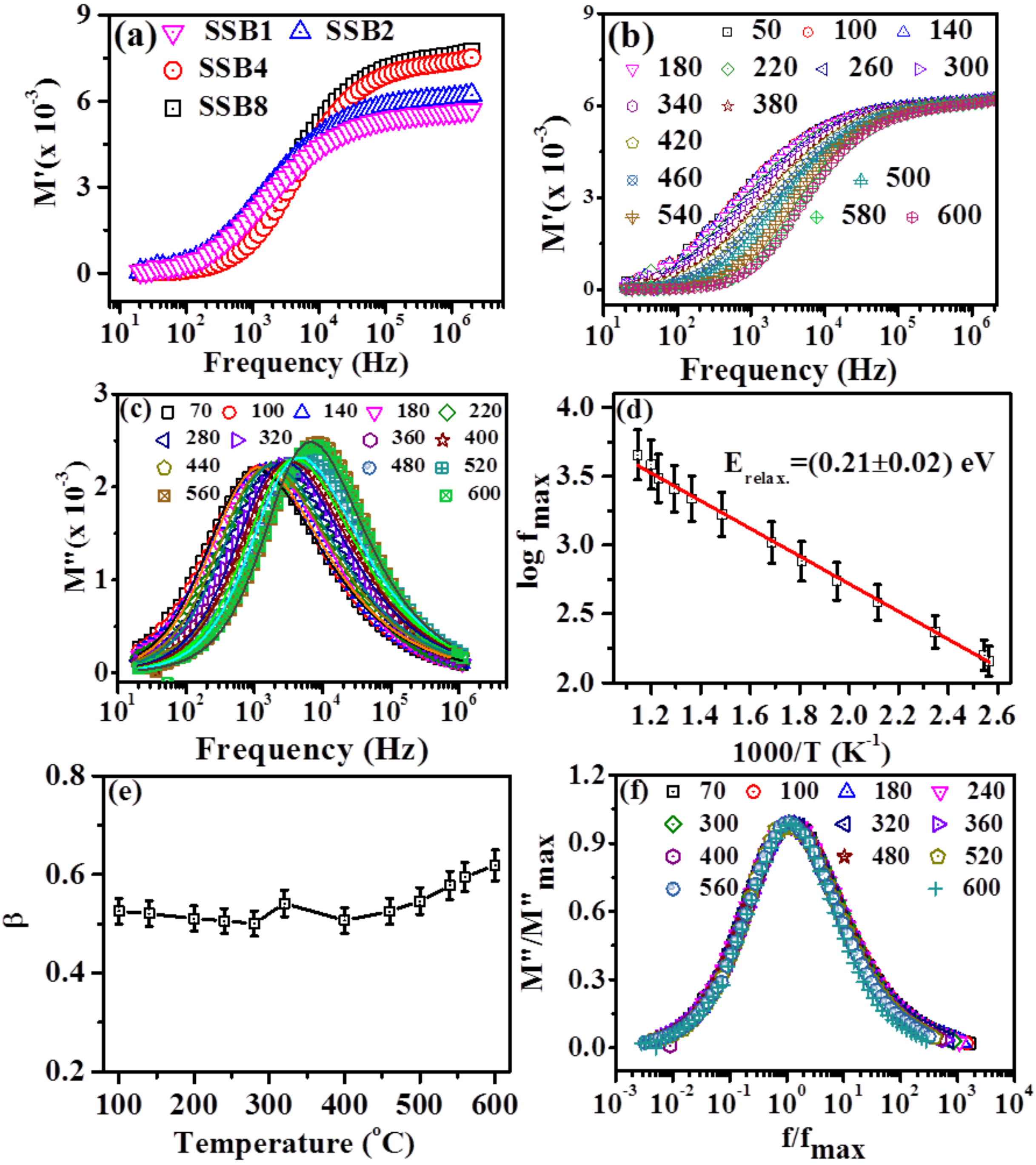

Figure 4.9 (a) Real part of modulus M' with frequency for all compositions at 400°C (b) Variation of Real part of modulus M' with frequency at several temperatures (c) Variation of Imaginary part M'' with frequency at several temperatures fitted with Eq. (11) (d) Arrhenius plot for relaxation frequency (e) Variation of KWW parameter with temperature (f) Scaled modulus vs. scaled frequency at several temperatures (Temperature in °C).

Furthermore, the distinction between the interfacial polarization occurred either due to electrode specimen interface or chemical microheterogeneity have carried out from the variation of real part of modulus (M'). The real part of modulus M' with respect to frequency is shown in Figure 4.9(a) at temperature 400^{o}C for all the samples. From Figure 4.9(a), it is observed that M' approaches zero towards lower frequencies thereafter a dispersion region in intermediate frequency range and then attained a maximum value at higher frequency. Almost zero value of M' at lower frequencies for all samples ruled out the polarization present at electrode-sample interface [183, 217]. Maximum value of M' at higher frequencies indicates the diminutive nature of forces governed by the mobility of charge carrier under the presence of field [189]. This study indicates that the dielectric properties has may be only contribution of the microhetrogeneity present in both grain and grain boundaries. Further, Figure 4.9(b) illustrates that the frequency dependence of M' at several temperatures for sample SSB2. From this plot, it is noticed that the dispersion region shifts towards higher frequency with increasing temperature suggests a temperature dependent relaxation process operative in the sample. For better understanding of dielectric relaxation process, imaginary part of modulus (M'') has been analysed with frequency and temperature. Figure 4.9(c) illustrates the variation of imaginary part of modulus M'' with frequency at different temperatures for sample SSB2. The typical spectrum shows that at the lower frequency, it show smaller value and increases with increasing frequency attains a maximum value M_{max} at a frequency f_{max}, thereafter decreases with further increase in frequency. In M'' vs. frequency plot, the frequency region towards lower side of f_{max} shows the range in which charge carriers are mobile over a long distance, and region higher side of frequency f_{max}, shows charge carriers being mobile over short distances confined to potential well. The region where the peak occurs indicates the presence of a transition from long range to short range mobility [223]. The position of peak M_{max} shifts towards higher frequency with increasing temperature which further indicates the presence temperature dependent relaxation process in the sample. To study the relaxation process involved in the sample, Kohlrauch –

Williams –Watts (KWW) function modified by Bergman has been employed to the imaginary part of Modulus (M'') as given by Eq. (3.8) [150, 183, 216, 217]. The solid line in Figure 4.8(c) shows fitting of Eq. (3.8) to the experimental data point. In order to understand the relaxation mechanism the parameters M''_{max}, β and ω_{max} are determined by fitting.

To study the thermally activated relaxation process, the logarithmic of f_{max} has been plotted with respect to the inverse of temperature for sample SSB2 are shown in Figure 4.8(d). The linear trend with negative slope indicates Arrhenius type relaxation process in the sample. The activation energy ($E_{relax.}$) determined by fitting Eq. (3.9) is found to be (0.22±0.02) eV. The value of β for SSB2 with respect to temperature is shown in Figure 4.9(e), value of β lies between 0.5-0.6 indicates a Non-Debye type relaxation process in the sample [183, 216, 217]. The value of β, activation energy for the relaxation process ($E_{relax.}$), τ_o and f_0 obtained for all samples are given in Table 4.3. Width of the $M''(f)$ peak determined by fitting of Gaussian distribution function and listed in Table 4.3. From Table 4.3, it is noticed that the value of β falls in between 0.49-0.64 which indicated the presence of non-Debye type relaxation processes in the entire sample. Moreover, the width of peak is found to be >1.14 decades, further reconfirms the nature of relaxation process is Non-Debye type. Since the range of temperature measurements and composition are wide, so the possibility of change in the relaxation mechanism can’t be ruled out. To check this possibility, the imaginary part of modulus (M'') is scaled by M_{max} and frequency axis is scaled by f_{max} (obtained from fitting), shown in Figure 4.9(f) for SSB2. The modulus spectrum at different temperatures is superimposed on a single master curve which confirms that the relaxation mechanism remains the same in entire range of temperature [189, 223].

In order to reconfirm the presence of Non-Debye type relaxation process, the Nyquist plots are generated for solid solutions. The Nyquist plot obtained from modulus (M'' vs. M') gives rise three semicircles corresponding to different type of contributions such as at lower frequency, it represents the contribution of electrode-specimen, in middle frequency, it represents contribution of grain boundary and even higher frequency, it represents a contribution of grains [157]. The Nyquist plot for all the samples at 400^{o}C is shown in Figure 4.10. A single semi-circular arc has been observed for all the samples. Moreover, the observed semi-circular arcs are depressed (centre lying below the M' axis) which suggests that there is distributions in relaxation time, consistent with the result obtained from M'' vs. $\log f$ plot. Further, it is observed that intercept $\left(\frac{C_o}{C_{total}}\right)$ for Nyquist plot increases and hence value of C_{total} decreases with increasing Ba which reconfirms that with incorporation of Ba at Sr site dielectric constant decreases. The value of capacitance (C_{total}) obtained from intercept is given in Table 4.4. As the order of capacitance is 10^{-12} F (Table 4.4), the observed semicircle can be assigned to bulk contribution [156].

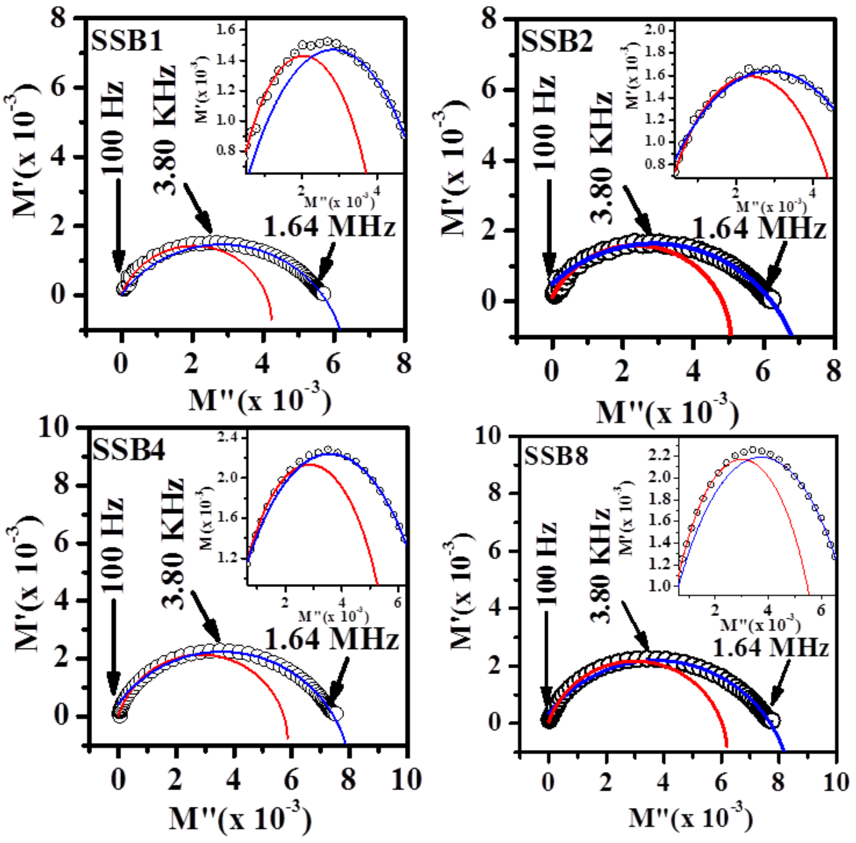

Figure 4.10 Nyquist plot for modulus fitted with cole-cole equation at 400^{o}C.

Table 4.3 Stretched Coefficient parameter (β), $C_{total,}$ FWHM and relaxation time obtained from $\boldsymbol{M''}(\boldsymbol{f})$ and parameter obtained from Eq. (13) for the solid solutions.

Physical Variable	**SSB1**		**SSB2**	**SSB4**	**SSB8**
β (KWW stretched Coefficient parameter)	100	0.53	0.56	0.53	0.49
	300	0.56	0.58	0.50	0.51
	600	0.55	0.64	0.62	0.55
C total from Nyquist plot (pF)	85.8		84.6	80.6	79.4
$E_{relaxation}$ (eV)	0.21		0.22	0.27	0.29
$E_{conduction}$ (eV)	0.22		0.25	0.32	0.35
Full Width at half maxima (FWHM) of M"(f) in decades	2.25		2.22	1.99	2.01
τ_o (in sec) x 10^{-9}	1.7		3.7	2.2	7.8

4.2.6.3 Conductivity Spectroscopy analysis

In order to elucidate the conduction behaviour and correlate with relaxation process discussed in preceding section, the frequency dependent conductivity of the samples has studied in frequency range 20 Hz to 2 MHz and in the temperature range of 250 to 600^{o}C. Below 250^{o}C the quality of data is not good due to the limitation of the instrument. The conductivity spectrum of sample SSB2 is shown in Figure 4.11(a). The ac conductivity spectra of sample illustrate two regions within the investigated temperature range. In the first region, the conductivity remains almost constant, known as dc conductivity (σ_{dc}) while in the second region, conductivity varies linearly with frequency, this part is known as ac conductivity (σ_{ac}). A clear crossover from frequency independent region to frequency dependent region has been observed in the conductivity spectra. The frequency at which crossover takes place is known as hopping frequency (ν_H). Furthermore, it is noticed that with increasing temperature, the value of dc conductivity and hopping frequency (ν_H) increases. The increase in the value of dc conductivity with temperature reflects the semiconducting behaviour of the samples. The shift in the value of hopping frequency (ν_H) towards higher value with increasing temperature shows that conduction phenomenon is thermally activated. The nature of frequency dependent conductivity of the samples can be represented by Johnscher's power law given by Eq. (2.36) [224].

In Figure 4.11(a), fitting of Johnscher's power law Eq. (2.36) to the experimental data points is shown by solid lines. Value of the parameters; σ_{dc}, ν_H , and n at different temperatures are extracted from the fitting. Variation of logarithmic of σ_{dc} against $1000/T$ for sample SSB2 is shown in Figure 4.11(b).

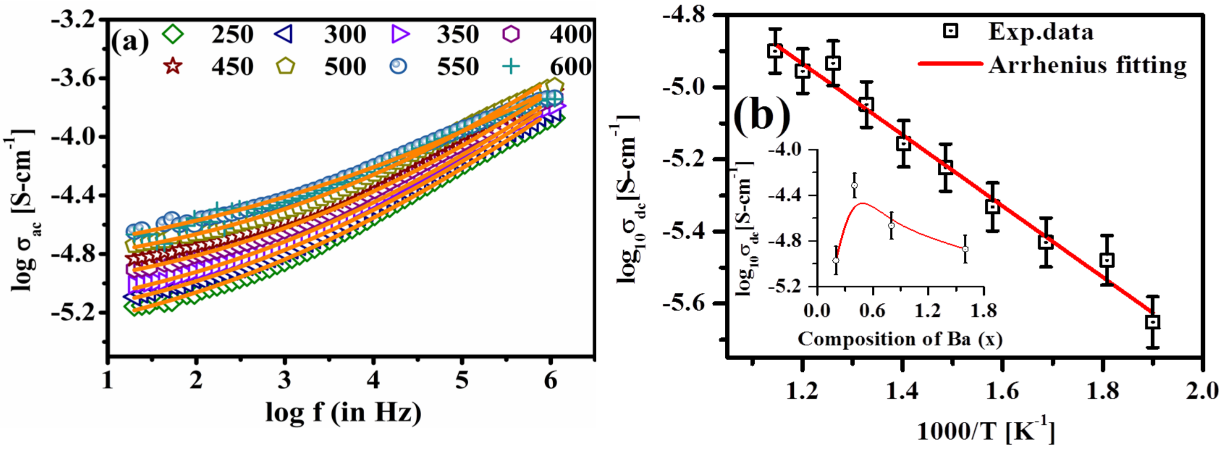

Figure 4.11 (a) Frequency-dependent conductivity spectra at different temperature fitted with Eq. (2.36) shown by solid line. (b) Variation of dc conductivity ($\boldsymbol{\sigma_{dc}}$) with inverse of temperature (Inset shows the compositional dependent dc conductivity at 400°C).

The activation energy for the migration of charged species is determined from Arrhenius relation given by Eq. (3.10). The activation energy for sample SSB2 is found to be (0.25±0.02) eV. The value of activation energy is obtained by Arrhenius relation for all samples are given in Table 4.3. The value of activation energy of all samples falls in between (0.22-0.35) eV, which reflects the nature of the sample is semiconductor. Both the end members, Ba_2SnO_4 (3.7eV) and Sr_2SnO_4 (4.8eV) are wide band gap (E_g) materials [225]. The value of activation energy for sample SSB8 has been found to be highest among the samples i.e. $E_{cond.}$ (0.35eV). Value of the activation energy is much less than the separation between the Fermi levels to the bottom of conduction band i.e., $0.5E_{g.}$ On account of small value of activation energy, possibility of any intrinsic conduction is ruled out. Hence conduction in these samples is extrinsic in nature might be due to the presence of defects. The e', $h^{\bullet}$, $V_o^{\bullet\bullet}$ and O_i'' are possible defects in the sample observed from XPS analysis. In this case, the lower value of activation energy indicates that the conduction is governed by hopping of electron between the mixed valence states of Sn^{4+}/Sn^{2+} ions. On comparing the value of $E_{cond.}$ with $E_{relax.}$, it is found that $E_{cond.}$ is approximately equal to the $E_{relax.}$ for all the samples. This implies that the source responsible for conduction and relaxation mechanism is the same at the local level or bulk level in the solid solutions. In respective of Ba composition, the activation energy for both processes relaxation and conduction is found to be increased with increasing Ba. In order to understand this variation the structural parameter can be taken into account. From Table 4.1, it has been noticed that the bond length between two Sn-sites along a, b direction almost equivalent to lattice parameter is increased with increasing the composition of Ba. The gradually increase in lattice parameter also increases the separation between the hopping sites and to transfer the electron in between hopping sites needs slight higher activation energy. In order to know the role of Ba on electrical conductivity, the compositional dependence of conductivity at 400°C is shown in the inset of Figure 4.12(b). On careful observation, it is noticed that the conductivity of solid solutions does not show any significant change with the incorporation of Ba. However, slight higher conductivity is observed for SSB2 sample may be due to presence of oxygen interstitial which make contribution in conductivity. With incorporation of Ba, it is presumed that no extra charge carrier has been generated to compensate the overall charge neutrality because it is a homovalent type of substitution and thus the conductivity is remains almost same for all samples.

Furthermore, the conduction mechanism can be explored using scaling described by various models like Ghosh scaling, Summerfield scaling and so on [226]. According to the Ghosh scaling, they have used dc conductivity (σ_{dc}) and hopping frequency (f_H) as a scaling parameter and given by scaling Eq. (2.38).

In this scaling process, the ac conductivity at a different temperature is scaled by σ_{dc} and the frequency is scaled by f_H as given by Eq. (2.38). The scaled plot for SSB2 at several temperatures is shown in Figure 4.12(a). The scaled conductivity and scaled frequency at 400°C for all solid solutions are shown in Figure 4.12(b). Clearly, the conductivity spectra of the solid solutions superimposed on a single master curve confirmed the validity of Time Temperature Superposition Principle (TTSP). This result is quite similar to the modulus formalism as discussed in Electric modulus formalism section.

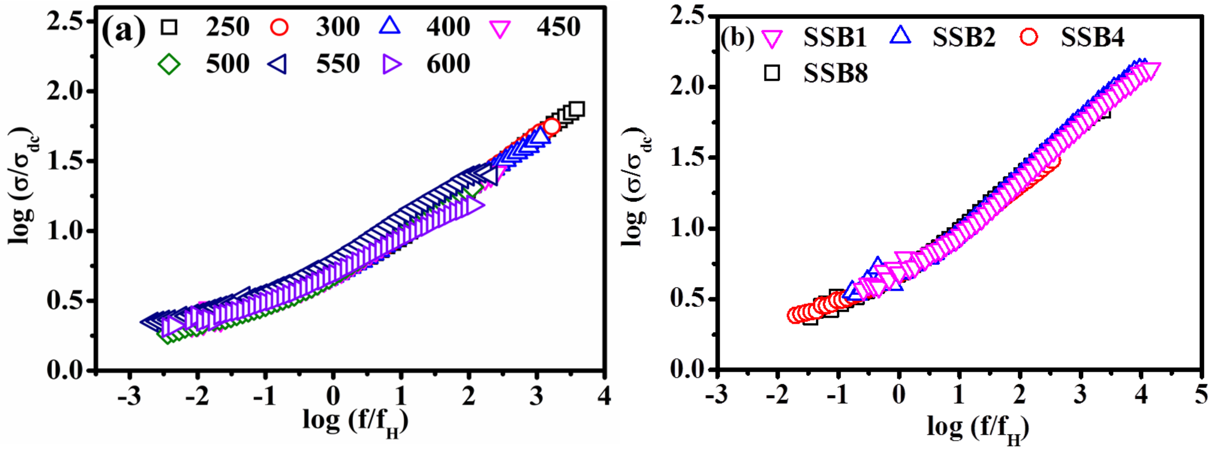

Figure 4.12 (a) Scaled conductivity with respect to scaled frequency at different temperature for sample SSB2 (b) Scaled conductivity with respect to scaled frequency for all solid solutions at 400°C.

We have also tried compositional scaling as described by the Summerfield for amorphous semiconductor, inorganic semiconductor and glass ceramic [193]. Summerfield defines the f_H as $\sigma_{dc} * T$ for conductivity spectra of various amorphous semiconductors, later on this is widely accepted by Rolling et al for sodium borate glasses [226]. Summerfield studied the compositional dependence of scaling behaviour and proposed that the conductivity spectra of $xNa_2O.(1-x)B_2O_3$ of different compositions can be superimposed on a single curve by taking the scaling frequency as $\frac{\sigma_{dc}\cdot T}{x}$. For this purpose, the scaled conductivity has been plotted against scaled frequency f_H as $\sigma_{dc} * T$ at 400°C for all samples as shown in Fig. 4.13(a). It has been observed that the conductivity spectra of all composition does not superimposed on a single master curve and suggests that the scaling parameter $\sigma_{dc} * T$ described by Summerfield is not a suitable scaling parameter for solid solutions. Rolling et al. used the scaling parameter hopping frequency (f_H) by $\frac{\sigma_{dc}\cdot T}{x}$ and plotted for all samples at 400°C in Figure 4.13(b). Moreover, it has been found by taking scaling frequency as $\frac{\sigma_{dc}\cdot T}{x}$ shows superposition of conductivity spectra on a single master curve. From compositional scaling, we have proposed that with the incorporation of Ba in the unit cell, the conduction mechanism remains the same for all solid solutions i.e., hopping of electron between the degenerate sites of Sn^{4+}/Sn^{2+}.

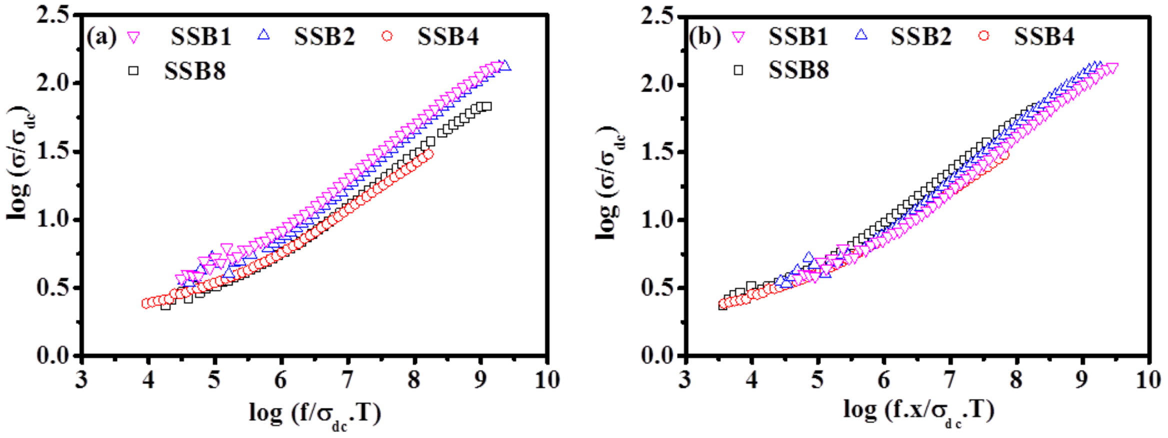

Figure 4.13 Summerfield scaling by taking as scaled frequency (a) $\sigma_{dc} * T$ (b) $\frac{\sigma_{dc}\cdot T}{x}$ for solid solutions.

4.3 Conclusions

The solid solutions of Ruddlesden Popper system $Sr_{2-x}Ba_xSnO_4$ (x=0, 0.20, 0.40, 0.80, 1.60, 2.00) were prepared by solid state ceramic route. The phase identification of the sample was performed using X - ray diffraction (XRD) analysis. Rietveld refinement of XRD was performed to determine the structural parameters. The lattice parameters are found to be increased with compositions of Ba; due to higher ionic radii of Ba than Sr. The multivalency of Sn, interstial oxygen and oxygen vacancy were probed by XPS analysis. The temperature dependence dielectric constant and dissipation factor show that dielectric constant decreased from 270 to 170 and dissipation factor from 0.2 to 0.5 at room temperature with increasing composition of Ba at 10 KHz. In this frequency range, orientation polarization present by respond of dipole ($Sn^{2+}{}_{Sn^{4+}}{}'' - V_o^{\cdot\cdot}$) with temperature. With increasing Ba composition, the interstitial oxygen makes a neutral pair and reduced the number of dipole which results decrease in dielectric constant. The relaxation mechanism explored by Kohlrauch-William-Watt (KWW) function applying to the modulus data. The values of KWW parameter β and width of $M''(f)$ for all samples indicated the presence of Non-Debye type relaxation process. Nyquist plot shows a depressed semicircle, the value of capacitance found to be order of 10^{-12} f indicated the bulk contribution present in sample. The AC conductivity of sample follows universal Johnscher's power law. The activation energy obtained for conduction process is approximately equal to the activation energy for relaxation process. This indicates that the conduction as well as relaxation process occurred in the samples are governed by similar source i.e., hopping of electron between Sn^{4+}/Sn^{2+}. Ghosh Scaling suggests that the conduction process remains same in entire temperature range. Moreover, the compositional scaling has been achieved by scaling parameter (f_H) as $\frac{\sigma_{dc}.T}{x}$. The obtained solid solutions possess a high value of dielectric constant (250) with low dissipation factor (0.2) makes it potential candidate for thermally stable capacitor application.